MATERIALS SCIENCE

Atomic-scale fatigue mechanism of ferroelectric tunnel junctions

Yihao Yang[1]†, Ming Wu[2,3]†, Xingwen Zheng[4]†, Chunyan Zheng[1], Jibo Xu[1], Zhiyu Xu[1], Xiaofei Li[1], Xiaojie Lou[2], Di Wu[5], Xiaohui Liu[4]*, Stephen J. Pennycook[3]*, Zheng Wen[1]*

Ferroelectric tunnel junctions (FTJs) are promising candidates for next-generation memories due to fast read/write speeds and low-power consumptions. Here, we investigate resistance fatigue of FTJs, which is performed on $Pt/BaTiO_3/Nb:SrTiO_3$ devices. By direct observations of the 5–unit cell–thick $BaTiO_3$ barrier with high-angle annular dark-field imaging and electron energy loss spectroscopy, oxygen vacancies are found to aggregate at the $Pt/BaTiO_3$ interface during repetitive switching, leading to a ferroelectric dead layer preventing domain nucleation and growth. Severe oxygen deficiency also makes $BaTiO_3$ lattices energetically unfavorable and lastly induces a destruction of local perovskite structure of the barrier. Ferroelectric properties are thus degraded, which reduces barrier contrast between ON and OFF states and smears electroresistance characteristics of $Pt/BaTiO_3/Nb:SrTiO_3$ FTJs. These results reveal an atomic-scale fatigue mechanism of ultrathin ferroelectric barriers associated with the aggregation of charged defects, facilitating the design of reliable FTJs and ferroelectric nanoelectronic devices for practical applications.

INTRODUCTION

Ferroelectric tunnel junctions (FTJs) are composed of two conductive electrodes separated by a nanometer-thick ferroelectric layer as a potential barrier, in which the polarization reversal alters the barrier profile and switches the junction conductance between a low (ON)– and a high (OFF)–resistance state, giving rise to the tunneling electroresistance (TER) (1–12). Functioned by the TER effect, FTJ devices exhibit a nondestructively resistive readout, which overcomes the main disadvantage of commercial ferroelectric random access memories (FeRAMs) (13). Therefore, enormous effort has been devoted to exploit the TER effect, and a number of excellent performances, such as giant TER ratios (R_{OFF}/R_{ON}) of several orders of magnitude (14–18), high write/erase speeds faster than a nanosecond (19), low-power consumptions of ~fJ/bit (6, 20), and good retentions more than 10 years (19, 21), have been realized recently in elaborately designed devices. These advances suggest the great potential of FTJs for next-generation nonvolatile memories.

However, the switching reliability, which is regarded as an essential prerequisite for practical applications of prototypical memories, has not been intensively investigated in FTJ devices yet. For FeRAMs, extensive studies have been made to explore the mechanisms of polarization fatigue, and the switching limits are optimized above ~10^9 cycles in Pb(Zr,Ti)O_3, BiFeO_3, BaTiO_3, and $Hf_{0.5}Zr_{0.5}O_2$ thin-film capacitors (22–26) as well as up to ~10^{12} cycles in Bi-layered perovskite oxides (27). For the other emerging nonvolatile memories, resistive random access memories (RRAMs),

the switching limits have also been optimized up to ~10^9 cycles by carefully controlling ion migration between the electrodes (28–32). However, in FTJs, even the repetitive switching of ultrathin ferroelectric films is very challenging presumably because of premature breakdown of the devices by bipolar switching in high electric fields. To date, only a few works have reported switching results with several orders of magnitude of cycles, which are summarized in fig. S1 for clarity. In these limited experiments, typical fatigue behaviors have been observed. Hwang *et al.* (33) reported in TiN/$Hf_{0.5}Zr_{0.5}O_2$/Ge FTJs that the conductance increases with increasing switching cycles, and the TER ratio is fatigued from ~10 to ~2 after ~10^6 cycles. In Pt/BaTiO_3/(La,Sr)MnO_3 devices, the pristine R_{OFF}/R_{ON} ratio of ~100 decreases with increasing fatigue cycles, and the bistable ON and OFF states become almost indistinguishable after ~5×10^5 cycles (34). In addition, markedly changed TER ratios have been observed in Co/BiFeO_3/(Ca,Ce)MnO_3 and Pt/BiFeO_3/Nb:SrTiO_3 FTJs when the switching cycles reach ~10^6 (35, 36). The reported switching limits in FTJs are much lower than that of the counterpart FeRAMs and RRAMs. Therefore, the resistance fatigue has become a main obstacle hampering further development of FTJs, but there is still no work addressing on the mechanism behind the degradation of TER properties with increasing write/erase cycles.

Here, we show a comprehensive study on resistance fatigue of FTJs, which is performed on Pt/BaTiO_3/Nb:SrTiO_3 tunnel junctions. In the devices, a reliable switching with a giant TER ratio of ~1.0×10^6 can be maintained up to ~3×10^6 cycles. The switching endurance is found also to be dependent on the pulse profile. However, after a finite number of write/erase cycles, obvious fatigue behavior still takes place. The mechanism of resistance fatigue is revealed at atomic scale based on direct observations by aberration-corrected scanning transmission electron microscopy (STEM) and piezoresponse force microscopy (PFM). During repetitive switching, the formation and aggregation of oxygen vacancies result in a ferroelectric dead layer at the Pt/BaTiO_3 interface, which blocks the nucleation and growth of reverse domains and increases the characteristic switching time and activation field of resistance switching. The oxygen deficiency also increases the formation energy of BaTi$O_{3-\delta}$ and eventually induces

[1]College of Physics and Center for Marine Observation and Communications, Qingdao University, Qingdao 266071, China. [2]State Key Laboratory of Electrical Insulation and Power Equipment and Frontier Institute of Science and Technology, Xi'an Jiaotong University, Xi'an 710049, China. [3]Department of Materials Science and Engineering, National University of Singapore, Singapore 117575, Singapore. [4]School of Physics, State Key Laboratory of Crystal Materials, Shandong University, Ji'nan 250100, China. [5]National Laboratory of Solid State Microstructures, Department of Materials Science and Engineering, Jiangsu Key Laboratory of Artificial Functional Materials and Collaborative Innovation Center for Advanced Materials, Nanjing University, Nanjing 210093, China.
*Corresponding author. Email: zwen@qdu.edu.cn (Z.W.); stephen.pennycook@cantab.net (S.J.P.); liuxiaohui@sdu.edu.cn (X.L.)
†These authors contributed equally to this work.

a lattice collapse of perovskite structure in the ultrathin barrier. As a result, the effective polarization and hence the TER ratio are markedly reduced in the fatigued Pt/BaTiO$_3$/Nb:SrTiO$_3$ device.

RESULTS
Microstructure and fatigue behavior
The microstructure of Pt/BTO/Nb:SrTiO$_3$ FTJs are characterized by atomic force microscopy (AFM) and high-angle annular dark-field (HAADF) images. Because of the Z-contrast nature of the HAADF imaging, the contrast of atom columns strongly depends on the atomic mass, and thus, the interface between BTO and Nb:SrTiO$_3$ (Nb:STO) can be distinguished (37). As shown in Fig. 1 (A and B), the 5–unit cell (u.c.)–thick BTO barrier exhibits an atomically smooth topography and sharp interfaces with the Pt and Nb:STO electrodes due to the cube-on-cube epitaxial growth. Figure 1C plots the out-of-plane and in-plane lattice spacing of the BTO/Nb:STO. As shown, the BTO barrier is almost fully strained on the Nb:STO with a tetragonality of ~1.06, indicating a robust room temperature ferro-electricity. By switching the BTO polarization, the Pt/BTO/Nb:STO

FTJ devices can exhibit nonvolatile ON and OFF states because of the modulation of Schottky barrier at the BTO/Nb:STO interface via the ferroelectric field effect (14, 15). The resistance-voltage (R-V) hysteresis loops are demonstrated in fig. S2 for clarity.

Figure 1D demonstrates the fatigue behavior of Pt/BTO/Nb:STO FTJs. The pulse waveform for collecting the resistance-cycle (R-N) curves is depicted in the inset. As shown, the bipolar pulse sequence (blue) with a certain number of cycles is used to repeatedly switch the devices. The ON and OFF states after the cycling are read by +0.3 V in the following readout sequence (red). The write voltages are set to −4.0 and +3.0 V according to the R-V hysteresis loops, which yields a saturated switching with the R_{OFF}/R_{ON} ratio of ~1.0 × 10^6. As shown in Fig. 1D, the resistance fatigue is dependent on the write pulse width (t). At t = 0.1 ms, the pristine R_{OFF}/R_{ON} ratio can be maintained up to ~3 × 10^6 cycles, while the device starts to be fatigued at ~1 × 10^3 cycles when the pulse width is increased to 100 ms. Figure 1E plots the onset cycle numbers of fatigue at various pulse widths, in which a linear relation is observed in the log$N$ versus log$t$ plot, suggesting that the resistance fatigue may be alleviated by decreasing t. In addition, the resistance fatigue is also found to be
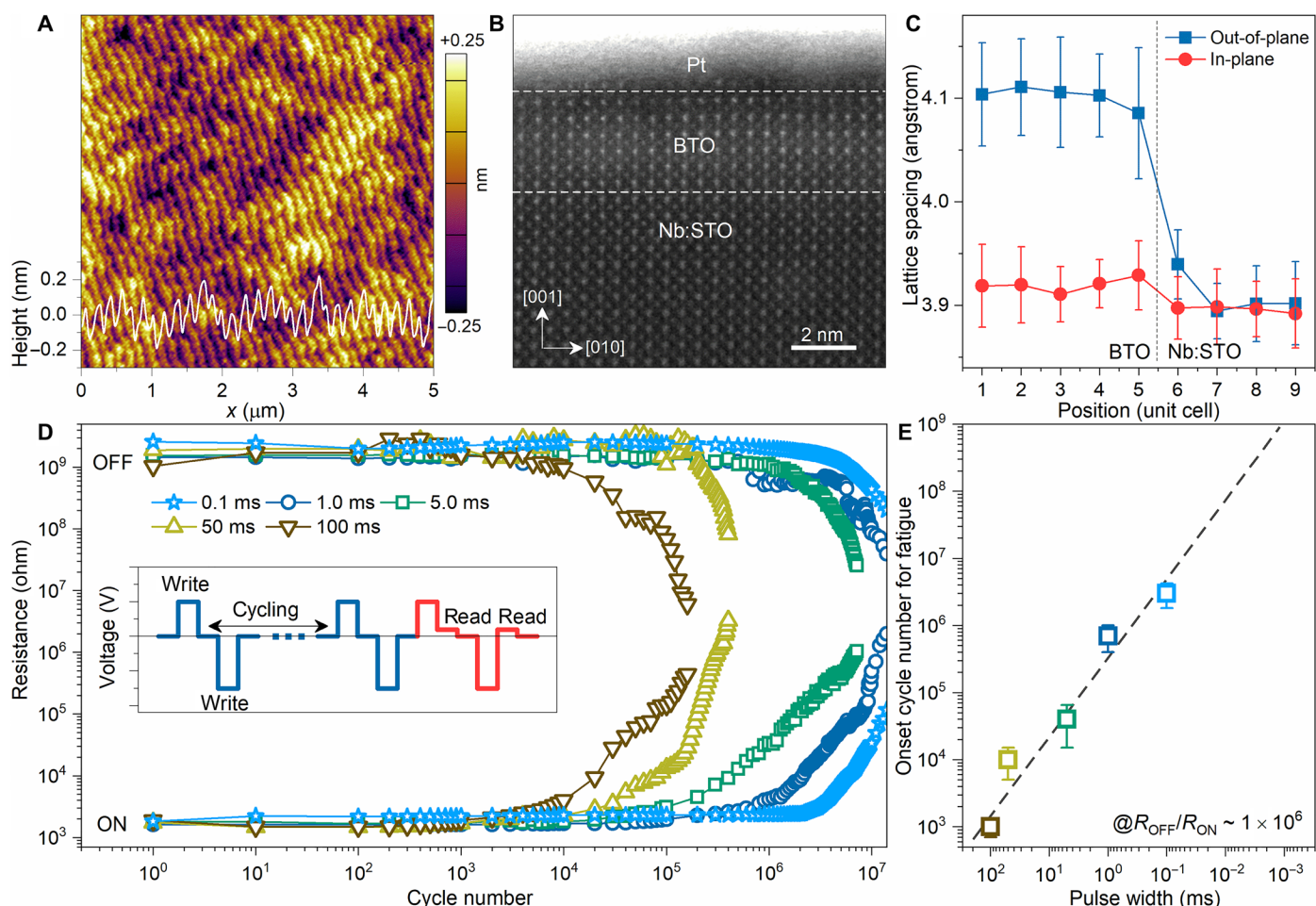
Fig. 1. Microstructure and resistance fatigue. (**A**) AFM surface topography of the 5-u.c.-thick BTO/Nb:STO heterostructure. (**B**) HAADF-STEM image of the Pt/BTO/Nb:STO FTJ device. (**C**) In-plane and out-of-plane lattice spacing of the BTO/Nb:STO heterostructure measured from the top of BTO down to the inside of Nb:STO, where the dashed line indicates the BTO/Nb:STO interface. (**D**) Resistance-cycle (R-N) curves of the ON and OFF states measured at various pulse widths. The inset depicts the pulse sequence for the fatigue measurement. (**E**) The onset cycle numbers for fatigue extracted from the R-N curves.

dependent on the write voltage (fig. S3). However, after finite numbers of switching cycles, severe fatigue behaviors still take place, in which the ON and OFF states are rapidly relaxed with the R_{OFF}/R_{ON} ratios reduced by as high as five orders of magnitude, as shown in Fig. 1D.

Atomic-scale observation of resistance fatigue

To reveal origins responsible for the resistance fatigue, we analyze atomic structures of the Pt/BTO/Nb:STO FTJs before and after the fatigue measurement by the HAADF imaging, as demonstrated in Fig. 2 (A and C). In comparison with the pristine Pt/BTO/Nb:STO, the fatigued device exhibits notable changes in the BTO barrier, in which two kinds of structures, named as regions A and B, are observed. In region A, the positions of A-site Ba and B-site Ti of perovskite BTO can be read from the clear contrast. However, these contrasts disappear in region B, suggesting the destruction of local perovskite structure. More information about the HAADF images over a large scale is shown in fig. S4 for clarity.

Figure 2 (E to G) demonstrates electron energy loss spectroscopy (EELS) spectra of Ti-$L_{2,3}$ edges of the pristine and regions A and B

of fatigued BTO barriers, respectively. Each EELS analysis includes the spectra acquired from the top and middle layers of the BTO barrier, as well as from the Nb:STO electrode, as indicated by the color boxes in Fig. 2 (B and D). It is well known that the energy splitting between t_{2g} and e_g in Ti-$L_{2,3}$ edges is a feature of Ti^{4+}, which results in four peaks in the EELS spectrum (37–39). For Ti^{3+}, there is no t_{2g}-e_g splitting, and only two peaks were observed, according to the EELS spectrum of LaTiO$_3$ (40). As shown in Fig. 2E, the pronounced peak splitting is observed in the L_2 and L_3 edges of BTO barrier and Nb:STO electrode, suggesting that Ti^{4+} ions are predominant in the pristine Pt/BTO/Nb:STO tunnel junction. After the fatigue measurement, although the Nb:STO still exhibits four peaks in EELS spectra, the t_{2g}-e_g splitting becomes weak in the $L_{2,3}$ edges of both regions A and B, indicating the presence of Ti^{3+} ions in the BTO barrier. The reductions of t_{2g}-e_g splitting have also been observed in ultrathin Pb(Zr,Ti)O$_3$/STO heterostructures and PbTiO$_3$/STO multilayers and ascribed to the existence of oxygen vacancies (38, 39). The generation of oxygen vacancies presumably result from an ionization effect of electrons emitted from the electrodes during electrical cycling, which weakens the Ti-O chemical bonds, and hence, the oxygen
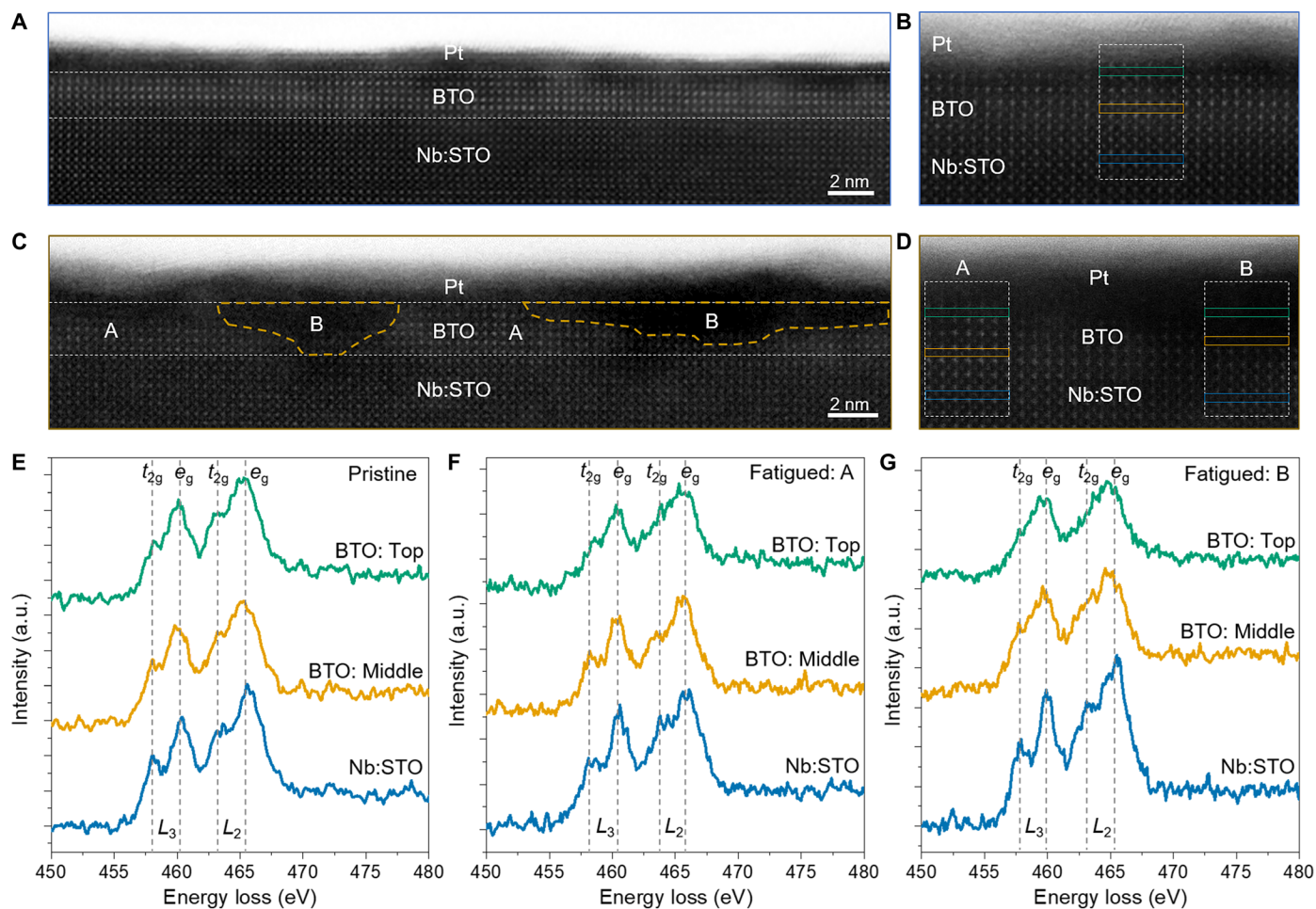
Fig. 2. Atomic structure and Ti ionic valence state of BTO barriers. HAADF-STEM images for the (**A** and **B**) pristine and (**C** and **D**) fatigued Pt/BTO/Nb:STO FTJs. In (C), region A (B) indicates the BTO barrier with (without) perovskite lattices after the fatigue measurement. EELS spectra of Ti-$L_{2,3}$ edges for the (**E**) pristine and (**F**) regions A and (**G**) B of fatigued BTO barriers, corresponding to the three areas indicated by the green, yellow, and blue rectangle boxes, respectively, for each region in (B) and (D). a.u., arbitrary units.

ions have a possibility to escape from the BTO lattices. At the same time, the Ti^{4+} is reduced to the Ti^{3+}. As shown in Fig. 2F, the reduction of t_{2g}-e_g splitting is mainly observed at the top layer of the BTO barrier, suggesting the aggregation of oxygen vacancies at the interface of Pt/region A because there is a huge difference in oxygen concentration between the BTO and the Pt electrode. In region B, the oxygen vacancies are increased and diffused over the whole region of BTO barrier, as indicated by the further weakened t_{2g}-e_g splitting in the top and middle EELS spectra in Fig. 2G. Note that the BTO lattice contrast is also absent in region B (Fig. 2C). The atomic-scale behavior of resistance fatigue can be understood as the following. During repetitive switching, the oxygen vacancies are formed and aggregated at the top of the BTO barrier in a finite thickness, which results in a ferroelectric dead layer in region A. With increasing cycles, more oxygen ions escape and the concentration of oxygen vacancies is increased. The perovskite BTO lattices cannot be maintained with the severe oxygen deficiency, and the contrasts of A-site Ba and B-site Ti disappear correspondingly. Region B is thus observed. As indicated by the region boundaries in Fig. 2C, region B grows gradually from top to bottom inside the fatigued BTO barrier. In addition, with increasing width and voltage of write pulse, the possibility for oxygen escape is increased because of more electrons are emitted from electrodes, resulting in the fast increase of the concentration of oxygen vacancies and thus earlier onset of resistance fatigue in the Pt/BTO/Nb:STO devices, as shown in Fig. 1D and fig. S3.

The oxygen vacancy–induced lattice destruction is further understood by calculating the energy of BTO$_{3-\delta}$ systems with first principles. As shown in fig. S5, the formation energy of BTO$_{3-\delta}$ increases monotonically with increasing δ. At $\delta = 0.5$, which means that the valence state of Ti ions is +3, close to the observations in EELS spectra of region B, the energy of BTO$_{2.5}$ is even beyond the enthalpy of formation of the BaO + TiO$_2$ system. These suggest that the BTO becomes energetically unfavorable with the oxygen deficiency. To lower the increased energy, the lattices have to be distorted, which may result in the destruction of perovskite structure. There are two possible ways for the lattice collapse of the oxygen-deficient BTO under pulse cycling: (i) decomposition to the parent oxides, such as BaO, TiO$_{2-\delta}$, and Ti$_2$O$_3$, as suggested by the calculations, and (ii) transformation to amorphous BTO because oxygen vacancy–induced amorphization has been experimentally observed in BTO nanocrystals (41) and theoretically simulated in bulk BTO by molecular dynamics (42). No matter which situation takes place, the consequence is the loss of ferroelectricity in region B.

Ferroelectric characterization of resistance fatigue

Ferroelectric properties of Pt/BTO/Nb:STO devices are measured by PFM. Considering that the BTO barrier is only 5 u.c. in thickness, the fatigue-induced change in piezoresponse signals may be smeared by the high ductility of the Pt top electrode. We therefore mechanically exfoliated the Pt electrode and performed PFM measurements directly on the BTO surface. Figure 3A shows the topography of Pt/BTO/Nb:STO after exfoliation of the Pt electrode, in which a step-terrace surface is observed, suggesting that there is no damage on the BTO barrier. It is also worth noting that the lateral size of conductive tips is ~30 nm in diameter, which is much larger than the size of regions A and B observed in Fig. 2C. Therefore, the piezoresponse signals of fatigued BTO barriers should be the average of regions A and B underneath the tip, as schematically depicted

in Fig. 3B. The ferroelectric properties of BTO barriers are characterized by PFM hysteresis loops collected from 5 × 5 grid positions over an area of 5 μm by 5 μm. The phase and amplitude loops of the pristine, the lightly fatigued, and the heavily fatigued devices are shown in fig. S6. For the BTO barrier with robust ferroelectricity, the polarization switching gives rise to a 180° phase contrast at a dc bias of 0 V and a butterfly-type amplitude loop with coercive voltages of ~+/−3.0 V in the saturated PFM loops, as shown in Fig. 3F. By mapping the phase contrast (ΔPhase) over the 5 × 5 grid positions, the spatial distribution of ferroelectricity of the BTO barrier can be demonstrated. As shown in Fig. 3C, the pristine BTO barrier is uniform with switchable polarization, in which almost all PFM loops have the 180° phase contrast. In the fatigued devices, pinned PFM loops are observed, in which both the phase contrast and the coercivity character are decreased and even indistinguishable (fig. S6). The loops with ΔPhase of ~90° and ~10° are shown in Fig. 3 (G and H) for clarity. The degraded pizeoresponse signals can be ascribed to the ferroelectric dead layers, in which the domain switching is blocked, or to the destruction of perovskite BTO lattices, which results in the loss of ferroelectricity. Figure 3 (D and E) demonstrates the phase contrast mappings of the lightly and heavily fatigued devices, respectively. As shown, the BTO barrier becomes more and more inhomogeneous with increased areas that have degraded ferroelectricity or are even nonferroelectric. Therefore, the effective polarization of BTO barrier is reduced with increasing switching cycles.

Simulation of resistance fatigue

To further understand the atomic-scale mechanism, we build an equivalent circuit according to the STEM and PFM observations, in which the resistance fatigue can be well reproduced. As demonstrated in Fig. 4A, the ferroelectric dead layer and the destructed BTO barrier, that is, the Pt/region B/Nb:STO, are represented by the series (R_S) and the parallel (R_P) resistors, respectively. The part that still has switchable polarization in region A is denoted by a pristine Pt/BTO/Nb:STO FTJ, which is in series with R_S. Note that the aggregation of oxygen vacancies makes the resistivity of the ferroelectric dead layer smaller than that of the BTO barrier itself. The resistance of R_S is set below the ON state. For the Pt/region B/Nb:STO, the Nb:STO surface may still be depleted by electrons because of the contact potential with the high work function Pt electrode. The Schottky barrier, however, should be lower than that of the OFF state because there is no polarization in region B (15). The resistance of R_P is thus set between the ON and OFF states. With increasing switching cycles, the concentration of oxygen vacancies increases in the BTO barrier. As a result, the thickness of ferroelectric dead layer increases, which is denoted by the increase of R_S resistance, and more region B appears between the Pt and Nb:STO, which can be regarded as the increase of parallel resistors in the equivalent circuit and hence denoted by the decrease of R_P resistance. As shown in Fig. 4B, by varying R_S from 100 to 500 ohm and R_P from 10^8 to 10^6 ohm, the memory window of the R-V hysteresis loop is gradually narrowed from R_{OFF}/R_{ON} of ~1.0×10^6 to less than 10, in good agreement with the observed resistance fatigue of Pt/BTO/Nb:STO devices.

DISCUSSION

Now, we discuss the fatigue-induced degradation in TER characteristics. Figure 5 (A to C) demonstrates transport characters and barrier profiles of the pristine and fatigued Pt/BTO/Nb:STO FTJs (see
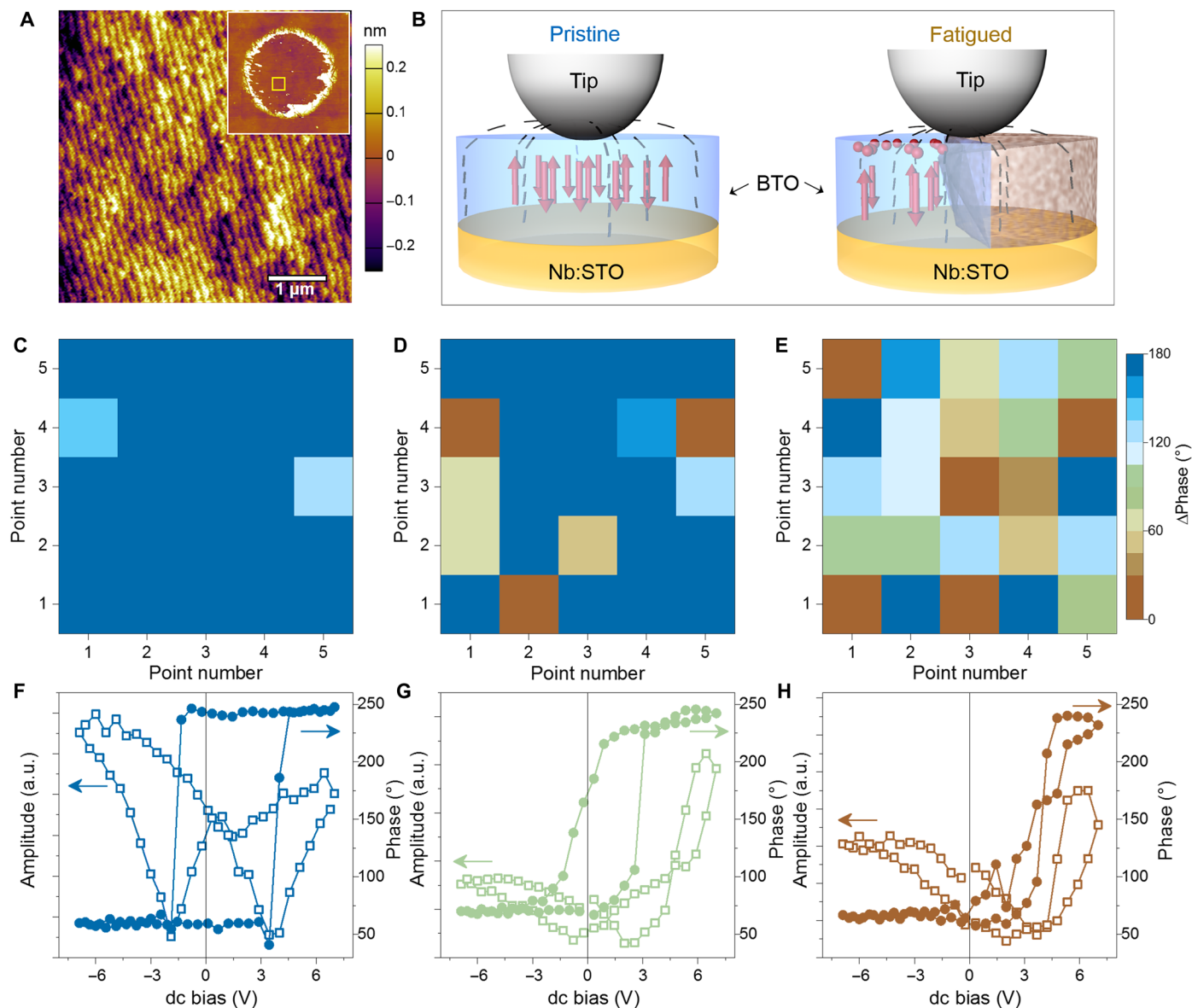
Fig. 3. Ferroelectric properties. (**A**) AFM topography of the Pt/BTO/Nb:STO device after the top Pt electrode is mechanically exfoliated. The inset shows the topography of the Pt electrode after exfoliation. (**B**) Schematic diagrams of the PFM measurements on the pristine and the fatigued BTO barriers, respectively, in which the red arrows and balls denote polarizations and oxygen vacancies, respectively, and the black dashed lines represent the electrical field underneath the conductive tip. In the fatigued BTO barrier, regions A and B are denoted by blue and brown colors. Phase contrast mappings of the PFM hysteresis loops collected at 5 × 5 grid positions of BTO barriers in (**C**) the pristine, (**D**) the lightly fatigued, and (**E**) the heavily fatigued Pt/BTO/Nb:STO FTJs, in which the color represents ΔPhase at dc bias = 0 V. Typical PFM hysteresis loops in the color mappings for ΔPhase of (**F**) ~180°, (**G**) ~90°, and (**H**) ~10°, respectively.
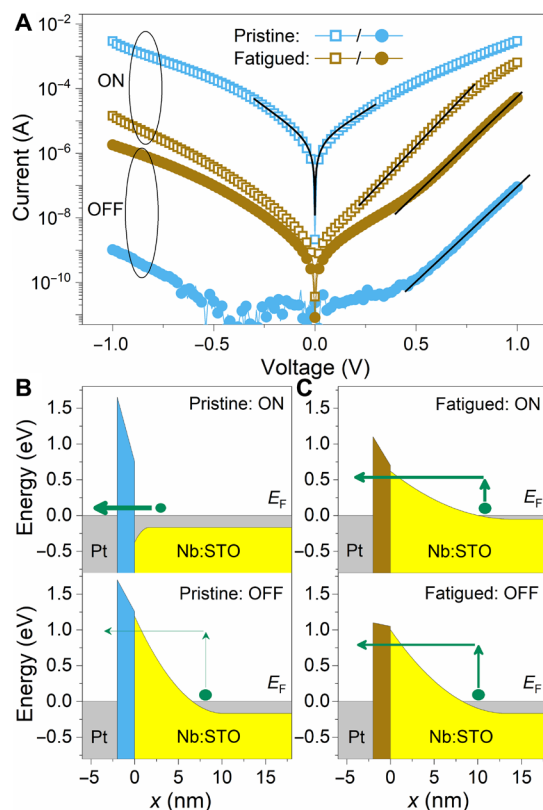
Materials and Methods for detailed information about the transport analyses and barrier profile calculations). In the pristine device, the polarization reversal in BTO barrier switches the Nb:STO surface between an accumulation and a depletion state. In the ON state with the BTO polarization toward the Nb:STO electrode, the interfacial Schottky barrier that is derived from the contact potential between Pt and Nb:STO is completely annihilated by accumulated electrons because of the positive ferroelectric bound charges. There is only the 5-u.c.-thick BTO barrier in the Pt/BTO/Nb:STO tunnel junction (Fig. 5B), which allows direct tunneling of electrons at the

Fermi level (E_F) and yields a large conductance, as observed in the current-voltage (I-V) curve in Fig. 5A. In the OFF state with the polarization switched against the Nb:STO, the negative ferroelectric bound charges at the BTO/Nb:STO interface enhance the Schottky barrier. The strong Schottky barrier, which is ~1.17 eV in height and ~9.5 nm in width, dramatically increases the effective barrier width at E_F and hence shut down the direct tunneling. The electrons have to be thermally emitted to an energy above E_F and then tunnel through the residual barrier (Fig. 5B), i.e., the thermally assisted tunneling. The conductance is thus substantially suppressed in the OFF state
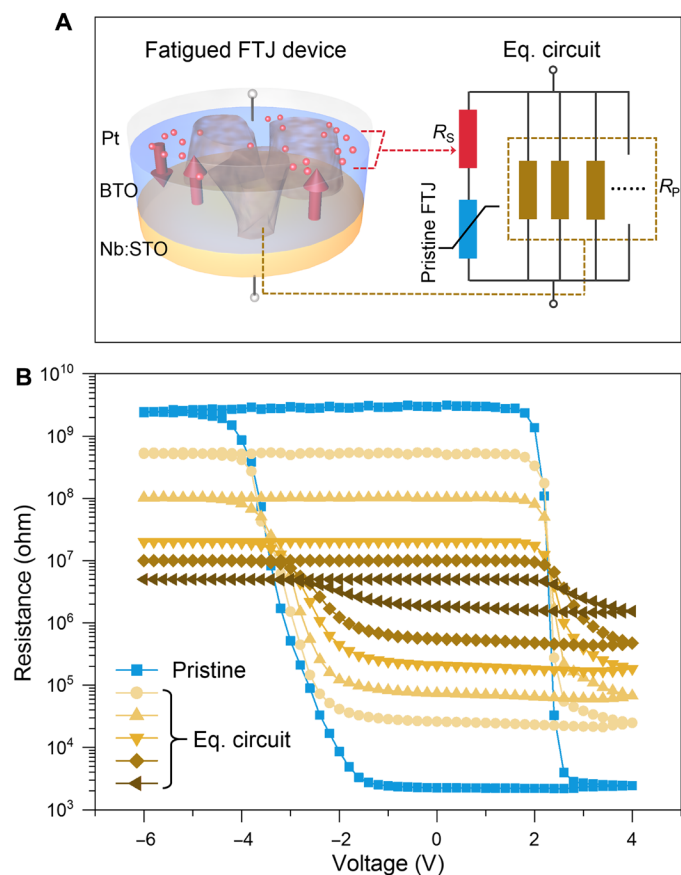
Fig. 4. Equivalent circuit for reproducing the resistance fatigue. (**A**) Schematics for the fatigued Pt/BTO/Nb:STO tunnel junction and the equivalent (Eq.) circuit built by a pristine Pt/BTO/Nb:STO and two variable resistors connected in series (R_S) and in parallel (R_P), respectively. (**B**) R-V hysteresis loops of the pristine device and the equivalent circuit with varying resistance of R_S and R_P. In the R-V hysteresis loops of Eq. circuit, the R_{OFF}/R_{ON} ratio is gradually reduced by increasing R_S, which means thickness increase of the ferroelectric dead layer in the BTO barrier and decreasing R_P, which denotes that more region B appears between the Pt and Nb:STO.

Fig. 5. Transport characters and barrier profiles. (**A**) ON and OFF current-voltage (I-V) curves of the pristine and fatigued Pt/BTO/Nb:STO FTJs. In (A), the black lines are fits to different transport models (see Materials and Methods). The ON and OFF barrier profiles of the (**B**) pristine and (**C**) fatigued devices, in which the green arrows denote the transport characters, are shown.

(Fig. 5A). After the fatigue measurement, the ferroelectric dead layer and the lattice collapse of perovskite structure reduce the effective polarization of the oxygen-deficient BTO barrier and degrade the ferroelectric modulation of the Schottky barrier. The barrier contrast between the ON and OFF states is thus weakened, as demonstrated in Fig. 5C. In the ON state, the positive ferroelectric bound charges are not large enough to make electron accumulation at the BTO/Nb:STO interface, and there still exists a considerable Schottky barrier due to the contact potential between Pt and Nb:STO (see Materials and Methods and Fig. 5B), which suppresses the direct tunneling in the fatigued device. The transport is thus changed to the thermally activated character, resulting in the decrease of the ON state conductance (Fig. 5A). For the OFF state, the polarization enhancement is reduced, and the Schottky barrier after fatigue measurement is only ~1.0 eV, which is lower than that of the pristine barrier (~1.17 eV). The thermally assisted tunneling is thus increased. Therefore, a markedly reduced TER ratio is observed in the fatigued Pt/BTO/Nb:STO device. Besides, it may not rule out the effects of oxygen vacancies on interfacial barriers and resistance

switching of the fatigued device with the oxygen-deficient BTO barrier (17, 43–45).

Switching characteristics of the Pt/BTO/Nb:STO device before and after fatigue measurement are demonstrated in Fig. 6. Here, we adopt the resistance formula $\frac{1}{R} = \frac{1-S}{R_{ON}} + \frac{S}{R_{OFF}}$ to calculate the normalized switched area (S) from the ON to the OFF state for the dynamics analysis (12). The actual switched areas of the 5-u.c.-thick BTO barrier as functions of pulse voltage and width are characterized in domain configurations by performing PFM mappings on the Pt electrode, as shown in fig. S7 and discussed in fig. S8 and table S1. Figure 6 (A and B) shows the change of S with increasing poling time (t_p) at various voltages. In the pristine device, the switching is sharp and easy to be saturated. However, the increase of S with t_p becomes slow, and the switching is smeared in the fatigued device. By analyzing the S-t_p curves with the nucleation-limited switching (NLS) model (see Materials and Methods), the switching characteristics that result from the nucleation and growth of domains in the BTO barriers are extracted and manifested as the distribution of switching time of various voltages, as demonstrated in Fig. 6C. Taking −5.0 V as an example, the pristine device exhibits a sharp distribution at the characteristic switching time (t_0) of ~2.5 × 10⁻⁸ s. By plotting t_0 versus $1/|E|$, the switching activation field (E_a) can be deduced on the basis of Merz's law $\left[t_0 \propto \exp\left(\frac{E_a}{|E|}\right) \right]$ (46), which is 16.13 V/nm as shown in
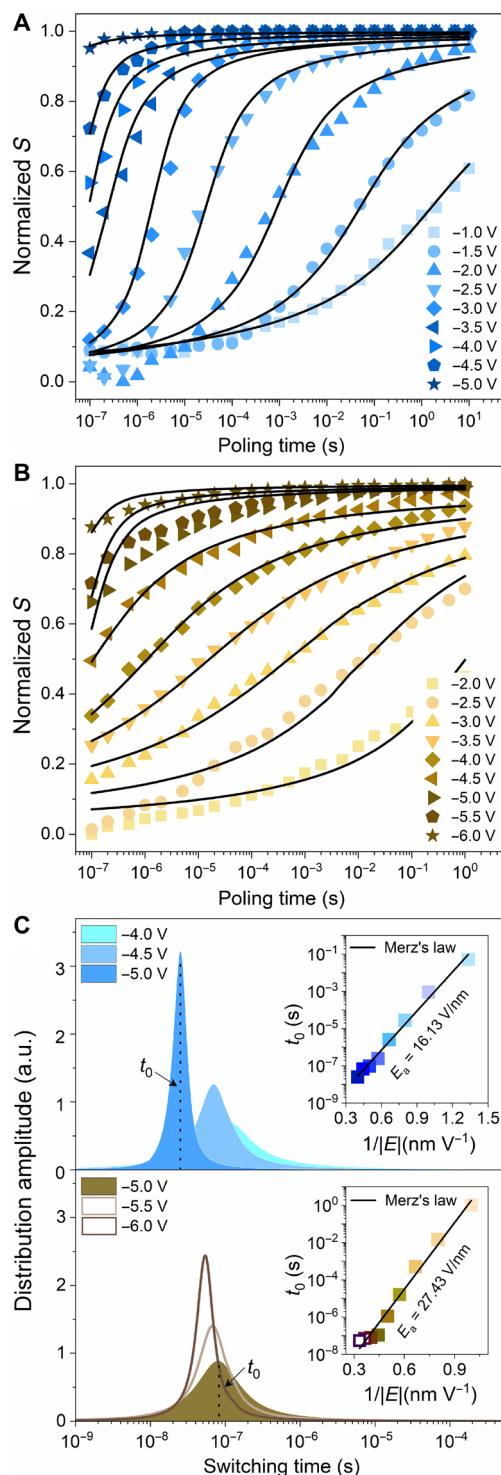
Fig. 6. Switching dynamics. Normalized switched areas (S) as functions of poling time and voltage for the (**A**) pristine and (**B**) fatigued Pt/BTO/Nb:STO FTJs, in which the black lines are fits to the NLS model (see Materials and Methods). (**C**) The pristine (top) and fatigued (bottom) Lorentzian distributions of switching time at different voltages extracted from the fits in (A and B), in which the insets plot characteristic switching time (t_0) versus the inverse of electric field ($1/|E|$), respectively. The solid lines in the insets are fits to Merz's law for extracting the switching activation field (E_a).

the inset. After the fatigue measurement, the domain switching is blocked because of the aggregation of charged oxygen vacancies in the BTO barrier. The switching time distribution of −5.0 V becomes very broad with increased t_0 to ~8.2×10^{-8} s. The sharp switching can only be observed by increasing the poling voltage to −6.0 V because stronger electrical stimuli are required to disperse the aggregated charges and set the blocked domains free. However, the t_0 (~5.4×10^{-8} s at −6.0 V) is still longer than that of the pristine device. Because of the increased t_0 and poling voltage, the fatigued Pt/BTO/Nb:STO exhibits a large E_a of 27.43 V/nm. Besides, the dispersion of oxygen vacancies by oversaturated voltages also leads to a partial rejuvenation of the fatigued device, as shown in the R-V hysteresis loops in fig. S2.

In summary, the mechanism of resistance fatigue has been revealed by direct observations of the BTO barrier with STEM and PFM, in which the formation of ferroelectric dead layer and the destruction of local perovskite lattices reduce the effective polarization and hence degrade the TER properties of the Pt/BTO/Nb:STO devices. These results shed light on the switching endurance issues of FTJs and ferroelectric nanoelectronic devices and may also be applicable to the complementary metal-oxide semiconductor–compatible HfO_2-based thin films as well, in which the ferroelectric degradation has been ascribed to the formation of oxygen-deficient interfacial layers near electrodes (*47*). In addition, the atomic-scale images of the aggregation of oxygen vacancies and the corresponding structure transform observed in the nanometer-thick BTO barriers under high electric fields of GV/m and strong electron tunneling, which are absent in traditional FeRAMs, provide new insights into the polarization fatigue, a long-standing problem for device reliability in the ferroelectric community.

It is also worth noting that the next-generation memory applications, such as the in-memory and brain-inspired computing, raise high requirements for device reliability, which is, ideally, ~10^{16} cycles for not only memory but also computing (*48*, *49*). There is still a tremendous scope to exploit the switching limits of FTJs. The present work, which clarifies the role of charged defects in resistance fatigue, facilitates the design of reliable ferroelectric tunneling devices and marks an important step toward future industrialization of the prototypical memories.

MATERIALS AND METHODS
Device preparation
The 5-u.c.-thick BTO thin films were epitaxially grown on (001) single-crystalline Nb:STO (Nb: 0.5 weight %) substrates by pulsed laser deposition using a KrF excimer laser (Coherent COMPexPro 201). Before the deposition, the Nb:STO substrates were etched by NH_4F buffered-HF solution and then annealed at 950°C for 1 hour in flowing O_2 to form a TiO_2 single-terminated step-terrace surface. The BTO films were deposited with a laser energy density of 2.5 J/cm^2 at 2-Hz repetition, keeping the substrate temperature at 750°C and the O_2 pressure at 1×10^{-2} mbar. Pt top electrodes of ~30 μm in diameter and ~100 nm in thickness were deposited on the surface of BTO/Nb:STO heterostructures by sputtering with a shadow mask to form the FTJ devices.

Characterizations
The cross-sectional TEM specimens were prepared by focused ion beam (FEI Versa workstation) with a Ga ion source. The HAADF-STEM

images were carried out at 200 kV by a JEOL ARM200CF microscope equipped with a cold field-emission electron gun, an ASCOR probe corrector and a Gatan Quantum ER spectrometer. The EELS spectra were collected with an energy dispersion of 0.25 eV per channel. Topographies and room-temperature ferroelectric properties were measured using an Asylum Research MFP-3D atomic force microscope. The PFM hysteresis loops were collected in the DART (dual ac resonance tracking) mode with triangle pulse waveforms applied to the conductive Pt/Ti-coated tips. The resistance switching and fatigue measurements of the Pt/BTO/Nb:STO FTJs were measured by a Keithley 2604B SourceMeter with homemade programs. Capacitances were recorded using an Agilent 4294A impedance analyzer at the frequency of 4 MHz and an oscillation level of 50 mV. The testing pulses were applied to the Pt electrodes, and the Nb:STO substrates were always grounded through indium ohmic contact pads.

Transport analyses and barrier profile calculations
In Fig. 5A, there are two kinds of transport characters in the I-V curves. For the pristine ON state, there is only the BTO barrier in the Pt/BTO/Nb:STO tunnel junction. The I-V curve is nonlinear and symmetric between the positive and negative biases, which can be described by the direct tunneling model based on a trapezoidal potential barrier (4). The current density (J) is given by

$$J = C \frac{\exp\left\{ \alpha(V) \left[\left(\Phi_2 - \frac{eV}{2} \right)^{3/2} - \left(\Phi_1 + \frac{eV}{2} \right)^{3/2} \right] \right\}}{\alpha^2(V) \left[\left(\Phi_2 - \frac{eV}{2} \right)^{1/2} - \left(\Phi_1 + \frac{eV}{2} \right)^{1/2} \right]^2}$$

$$\times \sinh\left\{ \frac{3}{2}\alpha(V) \left[\left(\Phi_2 - \frac{eV}{2} \right)^{1/2} - \left(\Phi_1 + \frac{eV}{2} \right)^{1/2} \right] \frac{eV}{2} \right\} \quad (1)$$

where $C = -(4em_n^*)/(9\pi^2\hbar^3)$ and $\alpha(V) = \left[4d(2m_n^*)^{\frac{1}{2}} \right]/[3\hbar(\Phi_1 + eV - \Phi_2)]$, $\Phi_1(\Phi_2)$ is the barrier height at the Pt/BTO (BTO/Nb:STO) interface, m_n^* is the effective electron mass, $\hbar$ is the reduced Planck constant, and d is the BTO barrier width (approximately 2.0 nm). By fitting the I-V curve with Eq. 1, the interface barrier heights are extracted, which are 1.60 and 0.74 eV at the Pt/BTO and BTO/Nb:STO interfaces, respectively, as shown in Fig. 5B.

For the pristine OFF state and the fatigued ON and OFF states, the transports are dominantly governed by Schottky barriers. Rectifying I-V curves are observed. The linear lg$I$-V plots at forward bias obey the thermally activated mechanism (50).

$$J_F = J_0 \exp(qV/nk_B T) \quad (2)$$

where J_F is the forward current density, J_0 the saturated current density, q is the electron charge, n is the ideality factor, k_B is the Boltzmann constant, and T is the absolute temperature. n extracted from the fits in Fig. 5A are 1.94, 2.94, and 2.74 for the pristine ON state and the fatigued ON and OFF states, respectively. The deviation of n from unity suggests the existence of thermally assisted tunneling across the barrier (51). In the Pt/BTO/Nb:STO FTJs, n can be written as $n = 1 + C_d/C_f$, where C_d and C_f are the high-frequency capacitances of the depleted region and the BTO barrier layer, respectively (52, 53). Therefore, by measuring the capacitance (C) of the whole junction, C_d can be deduced as nC because $\frac{1}{C} = \frac{1}{C_d} + \frac{1}{C_f}$. The voltage that drops over the depletion region (V_d) is correspondingly calibrated as V/n. The $C_d^{-2} - V_d$ plots are shown in fig. S9, which can be linearly fitted to

$C_d^{-2} = 2(V_{bi} - V_d)/q\varepsilon_0\varepsilon_r N_D A^2$ (ε_r is the relative dielectric constant of Nb:STO, and A is the junction area) and yields the doping concentration N_D of the Nb:STO and the build-in potential V_{bi} of the Schottky barriers. We therefore arrive at the depletion region width W_d as $W_d = \sqrt{2\varepsilon_0\varepsilon_r V_{bi}/qN_D}$. Taking $E_C(0) = V_{bi}$ and $E_C(\infty) = 0$ as the boundary conditions, the energy profile [$E_C(x)$] for the Schottky barrier as a function of the distance (x) from the BTO/Nb:STO interface to W_d can be deduced as follows (51)

$$E_C(x) = q(V_{bi} + \varphi_n) - \frac{q^2 N_D}{\varepsilon_0\varepsilon_r}\left(W_d x - \frac{x^2}{2} \right) \quad (3)$$

where φ_n is the difference between the conduction-band minimum (E_C) and the E_F of Nb:STO, defined as (E_C-E_F)/q, which is can be simply estimated using the effective mass of electrons m_n^* in Nb:STO

$$\varphi_n = \frac{E_F - E_C}{q} \approx \frac{k_B T}{q}\left[\ln\left(\frac{N_D}{N_C} \right) + 2^{-3/2}\left(\frac{N_D}{N_C} \right) \right] \quad (4)$$

$$N_C = 2\left(\frac{2\pi m_n^* k_B T}{h^2} \right)^{3/2} \quad (5)$$

where N_C is the density of states of the conduction band of Nb:STO and h is the Planck constant. The effective Richardson constant of Nb:STO in Schottky junctions is, in general, assumed to be 156 A/K^2 cm^2, which corresponds to $m_n^* = 1.3\ m_0$ (m_0, the electron mass). The deduced profiles of Schottky barriers are plotted in Fig. 5 (B and C) for the pristine OFF state and the fatigued ON and OFF states, respectively.

Switching dynamics analysis
The S-t curves are fitted by the NLS model, in which the resistance switching is regarded as inhomogeneous in different areas with independent dynamics (12, 54). S is given by

$$S = \int_{-\infty}^{+\infty}\left\{ 1 - \exp\left[-\left(\frac{t_p}{t_0} \right)^m \right] \right\} F(\log t_0)\, d(\log t_0) \quad (6)$$

where m is the effective dimension, equaling 2 for thin films, t_p is the poling time, t_0 is the characteristic switching time, and the distribution function is $F(\log t_0) = \frac{A_0}{\pi}\left[\frac{\Gamma}{(\log t - \log t_0)^2 + \Gamma^2} \right]$, adopting the Lorentzian distribution, in which A_0 is a normalization constant and Γ is the half width at half maximum (54).

REFERENCES AND NOTES
1. E. Y. Tsymbal, H. Kohlstedt, Tunneling across a ferroelectric. *Science* **313**, 181–183 (2006).
2. M. Y. Zhuravlev, R. F. Sabirianov, S. S. Jaswal, E. Y. Tsymbal, Giant electroresistance in ferroelectric tunnel junctions. *Phys. Rev. Lett.* **94**, 246802 (2005).
3. H. Kohlstedt, N. A. Pertsev, J. R. Contreras, R. Waser, Theoretical current-voltage characteristics of ferroelectric tunnel junctions. *Phys. Rev. B* **72**, 125341 (2005).
4. A. Gruverman, D. Wu, H. Lu, Y. Wang, H. W. Jang, C. M. Folkman, M. Y. Zhuravlev, D. Felker, M. Rzchowski, C. B. Eom, E. Y. Tsymbal, Tunneling electroresistance effect in ferroelectric tunnel junctions at the nanoscale. *Nano Lett.* **9**, 3539–3543 (2009).
5. V. Garcia, S. Fusil, K. Bouzehouane, S. Enouz-Vedrenne, N. D. Mathur, A. Barthelemy, M. Bibes, Giant tunnel electroresistance for non-destructive readout of ferroelectric states. *Nature* **460**, 81–84 (2009).
6. A. Chanthbouala, A. Crassous, V. Garcia, K. Bouzehouane, S. Fusil, X. Moya, J. Allibe, B. Dlubak, J. Grollier, S. Xavier, C. Deranlot, A. Moshar, R. Proksch, N. D. Mathur, M. Bibes,

A. Barthelemy, Solid-state memories based on ferroelectric tunnel junctions. *Nat. Nanotechnol.* **7**, 101–104 (2012).

7. V. Garcia, M. Bibes, Ferroelectric tunnel junctions for information storage and processing. *Nat. Commun.* **5**, 4289 (2014).

8. Z. Wen, D. Wu, Ferroelectric tunnel junctions: Modulations on the potential barrier. *Adv. Mater.* **32**, 1904123 (2019).

9. D. Pantel, S. Goetze, D. Hesse, M. Alexe, Reversible electrical switching of spin polarization in multiferroic tunnel junctions. *Nat. Mater.* **11**, 289–293 (2012).

10. A. Chanthbouala, V. Garcia, R. O. Cherifi, K. Bouzehouane, S. Fusil, X. Moya, S. Xavier, H. Yamada, C. Deranlot, N. D. Mathur, M. Bibes, A. Barthelemy, J. Grollier, A ferroelectric memristor. *Nat. Mater.* **11**, 860–864 (2012).

11. J. Li, C. Ge, J. Du, C. Wang, G. Yang, K. Jin, Reproducible ultrathin ferroelectric domain switching for high-performance neuromorphic computing. *Adv. Mater.* **32**, 1905764 (2020).

12. S. Boyn, J. Grollier, G. Lecerf, B. Xu, N. Locatelli, S. Fusil, S. Girod, C. Carretero, K. Garcia, S. Xavier, J. Tomas, L. Bellaiche, M. Bibes, A. Barthelemy, S. Saighi, V. Garcia, Learning through ferroelectric domain dynamics in solid-state synapses. *Nat. Commun.* **8**, 14736 (2017).

13. M. Dawber, K. M. Rabe, J. F. Scott, Physics of thin-film ferroelectric oxides. *Rev. Mod. Phys.* **77**, 1083–1130 (2005).

14. Z. Wen, C. Li, D. Wu, A. D. Li, N. B. Ming, Ferroelectric-field-effect-enhanced electroresistance in metal/ferroelectric/semiconductor tunnel junctions. *Nat. Mater.* **12**, 617–621 (2013).

15. Z. Xi, J. Ruan, C. Li, C. Zheng, Z. Wen, J. Dai, A. Li, D. Wu, Giant tunnelling electroresistance in metal/ferroelectric/semiconductor tunnel junctions by engineering the Schottky barrier. *Nat. Commun.* **8**, 15217 (2017).

16. H. Yamada, V. Garcia, S. Fusil, S. Boyn, M. Marinova, A. Gloter, S. Xavier, J. Grollier, E. Jacquet, C. Carretero, C. Deranlot, M. Bibes, A. Barthelemy, Giant electroresistance of super-tetragonal BiFeO₃-based ferroelectric tunnel junctions. *ACS Nano* **7**, 5385–5390 (2013).

17. J. K. Li, N. Li, C. Ge, H. Y. Huang, Y. W. Sun, P. Gao, M. He, C. Wang, G. Z. Yang, K. J. Jin, Giant electroresistance in ferroionic tunnel junctions. *iScience* **16**, 368–377 (2019).

18. F. Y. Bruno, S. Boyn, S. Fusil, S. Girod, C. Carretero, M. Marinova, A. Gloter, S. Xavier, C. Deranlot, M. Bibes, A. Barthelemy, V. Garcia, Millionfold resistance change in ferroelectric tunnel junctions based on nickelate electrodes. *Adv. Electron. Mater* **2**, 1500245 (2016).

19. C. Ma, Z. Luo, W. Huang, L. Zhao, Q. Chen, Y. Lin, X. Liu, X. Liu, Z. Chen, C. Liu, H. Sun, X. Jin, Y. Yin, X. Li, Sub-nanosecond memristor based on ferroelectric tunnel junction. *Nat. Commun.* **11**, 1439 (2020).

20. W. Huang, W. Zhao, Z. Luo, Y. Yin, Y. Lin, C. Hou, B. Tian, C.-G. Duan, X.-G. Li, A high-speed and low-power multistate memory based on multiferroic tunnel junctions. *Adv. Electron. Mater.* **4**, 1700560 (2018).

21. Z. Xi, Q. Jin, C. Zheng, Y. Zhang, C. Lu, Q. Li, S. Li, J. Dai, Z. Wen, High-temperature tunneling electroresistance in metal/ferroelectric/semiconductor tunnel junctions. *Appl. Phys. Lett.* **111**, 132905 (2017).

22. M.-G. Han, M. S. J. Marshall, L. Wu, M. A. Schofield, T. Aoki, R. Twesten, J. Hoffman, F. J. Walker, C. H. Ahn, Y. Zhu, Interface-induced nonswitchable domains in ferroelectric thin films. *Nat. Commun.* **5**, 4693 (2014).

23. S. H. Baek, C. M. Folkman, J.-W. Park, S. Lee, C.-W. Bark, T. Tybell, C.-B. Eom, The nature of polarization fatigue in BiFeO₃. *Adv. Mater.* **23**, 1621–1625 (2011).

24. X. Zou, L. You, W. G. Chen, H. Ding, D. Wu, T. Wu, L. Chen, J. L. Wang, Mechanism of polarization fatigue in BiFeO₃. *ACS Nano* **6**, 8997–9004 (2012).

25. Y. S. Kim, J. Y. Jo, D. J. Kim, Y. J. Chang, J. H. Lee, T. W. Noh, T. K. Song, J. G. Yoon, J. S. Chung, S. I. Baik, Y. W. Kim, C. U. Jung, Ferroelectric properties of SrRuO₃/BaTiO₃/SrRuO₃ ultrathin film capacitors free from passive layers. *Appl. Phys. Lett.* **88**, 072909 (2006).

26. Q. Luo, Y. Cheng, J. G. Yang, R. R. Cao, H. L. Ma, Y. Yang, R. Huang, W. Wei, Y. H. Zheng, T. C. Gong, J. Yu, X. X. Xu, P. Yuan, X. Y. Li, L. Tai, H. R. Yu, D. S. Shang, Q. Liu, B. Yu, Q. W. Ren, H. B. Lv, M. Liu, A highly CMOS compatible hafnia-based ferroelectric diode. *Nat. Commun.* **11**, 1391 (2020).

27. C. Dearaujo, J. D. Cuchiaro, L. D. Mcmillan, M. C. Scott, J. F. Scott, Fatigue-free ferroelectric capacitors with platinum electrodes. *Nature* **374**, 627–629 (1995).

28. Z. Wei, Y. Kanzawa, K. Arita, Y. Katoh, K. Kawai, S. Muraoka, S. Mitani, S. Fujii, K. Katayama, M. Iijima, T. Mikawa, T. Ninomiya, R. Miyanaga, Y. Kawashima, K. Tsuji, A. Himeno, T. Okada, R. Azuma, K. Shimakawa, H. Sugaya, T. Takagi, R. Yasuhara, K. Horiba, H. Kumigashira, M. Oshima, Highly reliable TaOₓ ReRAM and direct evidence of redox reaction mechanism. *IEEE Int. Electron Dev. Meet. Tech. Dig.* **293**, 5671467 (2008).

29. B. Chen, Y. Lu, B. Gao, Y. H. Fu, F. F. Zhang, P. Huang, Y. S. Chen, L. F. Liu, X. Y. Liu, J. F. Kang, Y. Y. Wang, Z. Fang, H. Y. Yu, X. Li, X. P. Wang, N. Singh, G. Q. Lo, D. L. Kwong, Physical mechanisms of endurance degradation in TMO-RRAM, in *2011 IEEE International Electron Devices Meeting (IEDM)* (IEEE, 2011), pp. 12.3.1–12.3.4.

30. H. Y. Lee, P. S. Chen, T. Y. Wu, Y. S. Chen, C. C. Wang, P. J. Tzeng, C. H. Lin, F. Chen, C. H. Lien, M. J. Tsai, Low power and high speed bipolar switching with a thin reactive Ti buffer layer in robust HfO₂ based RRAM, in *IEEE International Electron Devices Meeting* (IEEE, 2008), vol. 297, p. 5671467.

31. U. Chand, C. Y. Huang, J. H. Jieng, W. Y. Jang, C. H. Lin, T. Y. Tseng, Suppression of endurance degradation by utilizing oxygen plasma treatment in HfO₂ resistive switching memory. *Appl. Phys. Lett.* **106**, 153502 (2015).

32. C. Y. Chen, L. Goux, A. Fantini, S. Clima, R. Degraeve, A. Redolfi, Y. Y. Chen, G. Groeseneken, M. Jurczak, Endurance degradation mechanisms in TiN\Ta₂O₅\Ta resistive random-access memory cells. *Appl. Phys. Lett.* **106**, 053501 (2015).

33. J. Hwang, Y. Goh, S. Jeon, Effect of forming gas high-pressure annealing on metal-ferroelectric-semiconductor hafnia ferroelectric tunnel junction. *IEEE Electron Device Lett.* **41**, 1193–1196 (2020).

34. R. Guo, Z. Wang, S. W. Zeng, K. Han, L. S. Huang, D. G. Schlom, T. Venkatesan, Ariando, J. S. Chen, Functional ferroelectric tunnel junctions on silicon. *Sci. Rep.* **5**, 12576 (2015).

35. S. Boyn, S. Girod, V. Garcia, S. Fusil, S. Xavier, C. Deranlot, H. Yamada, C. Carretero, E. Jacquet, M. Bibes, A. Barthelemy, J. Grollier, High-performance ferroelectric memory based on fully patterned tunnel junctions. *Appl. Phys. Lett.* **104**, 052909 (2014).

36. W. J. Hu, Z. H. Wang, W. L. Yu, T. Wu, Optically controlled electroresistance and electrically controlled photovoltage in ferroelectric tunnel junctions. *Nat. Commun.* **7**, 10808 (2016).

37. M. Varela, J. Gazquez, S. J. Pennycook, STEM-EELS imaging of complex oxides and interfaces. *MRS Bull.* **37**, 29–35 (2012).

38. K. Du, M. Zhang, C. Dai, Z. N. Zhou, Y. W. Xie, Z. H. Ren, H. Tian, L. Q. Chen, G. Van Tendeloo, Z. Zhang, Manipulating topological transformations of polar structures through real-time observation of the dynamic polarization evolution. *Nat. Commun.* **10**, 4864 (2019).

39. M. Q. Li, X. X. Cheng, N. Li, H. J. Liu, Y. L. Huang, K. H. Liu, Y. H. Chu, D. P. Yu, L. Q. Chen, Y. Ikuhara, P. Gao, Atomic-scale mechanism of internal structural relaxation screening at polar interfaces. *Phys. Rev. B* **97**, 180103 (2018).

40. A. Ohtomo, D. A. Muller, J. L. Grazul, H. Y. Hwang, Artificial charge-modulation in atomic-scale perovskite titanate superlattices. *Nature* **419**, 378–380 (2002).

41. X. Tian, G. L. Brennecka, X. Tan, Structural instability in electrically stressed, oxygen deficient BaTiO₃ nanocrystals. *Adv. Funct. Mater.* **30**, 2004607 (2020).

42. Y. Ma, Y. X. Chen, Y. C. Zhou, Molecular dynamics simulations of the radiation induced structural changes in BaTiO₃. *Radiat. Eff. Defects Solids* **163**, 189–197 (2008).

43. C. Wang, K. J. Jin, Z. T. Xu, L. Wang, C. Ge, H. B. Lu, H. Z. Guo, M. He, G. Z. Yang, Switchable diode effect and ferroelectric resistive switching in epitaxial BiFeO₃ thin films. *Appl. Phys. Lett.* **98**, 192901 (2011).

44. M. Li, J. Zhou, X. S. Jing, M. Zeng, S. J. Wu, J. W. Gao, Z. Zhang, X. S. Gao, X. B. Lu, J. M. Liu, M. Alexe, Controlling resistance switching polarities of epitaxial BaTiO₃ films by mediation of ferroelectricity and oxygen vacancies. *Adv. Electron. Mater.* **1**, 1500069 (2015).

45. D. H. Martin, F. Gallego, J. Tornos, V. Rouco, J. I. Beltran, C. Munuera, D. S. Manzano, M. Cabero, F. Cuellar, D. Arias, G. S. Santolino, F. J. Mompean, M. G. Hernandez, A. R. Calzada, S. J. Pennycook, M. Varela, M. C. Muñoz, Z. Sefrioui, C. Leon, J. Santamaria, Controlled sign reversal of electroresistance in oxide tunnel junctions by electrochemical-ferroelectric coupling. *Phys. Rev. Lett.* **125**, 266802 (2020).

46. W. J. Merz, Domain formation and domain wall motions in ferroelectric BaTiO₃ single crystals. *Phys. Rev.* **95**, 690–698 (1954).

47. K. Y. Chen, P. H. Chen, R. W. Kao, Y. X. Lin, Y. H. Wu, Impact of plasma treatment on reliability performance for HfZrOₓ-based metal-ferroelectric-metal capacitors. *IEEE Electron Dev. Lett.* **39**, 87–90 (2018).

48. J. J. Yang, D. B. Strukov, D. R. Stewart, Memristive devices for computing. *Nat. Nanotechnol.* **8**, 13–24 (2013).

49. Q. Xia, J. J. Yang, Memristive crossbar arrays for brain-inspired computing. *Nat. Mater.* **18**, 309–323 (2019).

50. S. Suzuki, T. Yamamoto, H. Suzuki, K. Kawaguchi, K. Takahashi, Y. Yoshisato, Fabrication and characterization of Ba₁₋ₓKₓBiO₃/Nb-doped SrTiO₃ all-oxide-type schottky junctions. *J. Appl. Phys.* **81**, 6830–6836 (1997).

51. S. M. Sze, K. K. Ng, *Physics of Semiconductor Devices* (Wiley, ed. 3, 2007).

52. E. Mikheev, B. D. Hoskins, D. B. Strukov, S. Stemmer, Resistive switching and its suppression in Pt/Nb:SrTiO₃ junctions. *Nat. Commun.* **5**, 3990 (2014).

53. H. C. Card, E. H. Rhoderick, Studies of tunnel MOS diodes I. Interface effects in silicon Schottky diodes. *J. Phys. D Appl. Phys.* **4**, 1589–1601 (1971).

54. J. Y. Jo, H. S. Han, J. G. Yoon, T. K. Song, S. H. Kim, T. W. Noh, Domain switching kinetics in disordered ferroelectric thin films. *Phys. Rev. Lett.* **99**, 267602 (2007).

55. Z. Wen, L. You, J. L. Wang, A. D. Li, D. Wu, Temperature-dependent tunneling electroresistance in Pt/BaTiO₃/SrRuO₃ ferroelectric tunnel junctions. *Appl. Phys. Lett.* **103**, 132913 (2013).

56. L. Chen, T. Y. Wang, Y. W. Dai, M. Y. Cha, H. Zhu, Q. Q. Sun, S. J. Ding, P. Zhou, L. Chua, D. W. Zhang, Ultra-low power $Hf_{0.5}Zr_{0.5}O_2$ based ferroelectric tunnel junction synapses for hardware neural network applications. *Nanoscale* **10**, 15826–15833 (2018).

57. D. Y. Kusuma, P. Lee, Ferroelectric tunnel junction memory devices made from monolayers of vinylidene fluoride oligomers. *Adv. Mater.* **24**, 4163–4169 (2012).

58. Y. Goh, S. Jeon, The effect of the bottom electrode on ferroelectric tunnel junctions based on CMOS-compatible HfO_2. *Nanotechnology* **29**, 335201 (2018).

59. Z. P. Li, X. Guo, H. B. Lu, Z. L. Zhang, D. S. Song, S. B. Cheng, M. Bosman, J. Zhu, Z. L. Dong, W. G. Zhu, An epitaxial ferroelectric tunnel junction on silicon. *Adv. Mater.* **26**, 7185–7189 (2014).

60. J. B. Wu, H. Y. Chen, N. Yang, J. Cao, X. D. Yan, F. X. Liu, Q. B. Sun, X. Ling, J. Guo, H. Wang, High tunnelling electroresistance in a ferroelectric van der Waals heterojunction via giant barrier height modulation. *Nat. Electron.* **3**, 466–472 (2020).

61. H. J. Mao, P. X. Miao, J. Z. Cong, C. Song, B. Cui, J. J. Peng, G. Y. Wang, Y. G. Zhao, Y. Sun, L. R. Xiao, F. Pan, Interface-modification-enhanced tunnel electroresistance in multiferroic tunnel junctions. *J. Appl. Phys.* **116**, 053703 (2014).

62. P. Giannozzi, S. Baroni, N. Bonini, M. Calandra, R. Car, C. Cavazzoni, D. Ceresoli, G. L. Chiarotti, M. Cococcioni, I. Dabo, A. D. Corso, S. de Gironcoli, S. Fabris, G. Fratesi, R. Gebauer, U. Gerstmann, C. Gougoussis, A. Kokalj, M. Lazzeri, L. Martin-Samos, N. Marzari, F. Mauri, R. Mazzarello, S. Paolini, A. Pasquarello, L. Paulatto, C. Sbraccia, S. Scandolo, G. Sclauzero, A. P. Seitsonen, A. Smogunov, P. Umari, R. M. Wentzcovitch, QUANTUM ESPRESSO: A modular and open-source software project for quantum simulations of materials. *J. Phys. Condens. Matter* **21**, 395502 (2009).

63. P. Giannozzi, O. Andreussi, T. Brumme, O. Bunau, M. B. Nardelli, M. Calandra, R. Car, C. Cavazzoni, D. Ceresoli, M. Cococcioni, N. Colonna, I. Carnimeo, A. D. Corso, S. de Gironcoli, P. Delugas, R. A. DiStasio Jr., A. Ferretti, A. Floris, G. Fratesi, G. Fugallo, R. Gebauer, U. Gerstmann, F. Giustino, T. Gorni, J. Jia, M. Kawamura, H. Y. Ko, A. Kokalj, E. Küçükbenli, M. Lazzeri, M. Marsili, N. Marzari, F. Mauri, N. L. Nguyen, H. V. Nguyen, A. Otero-de-la-Roza, L. Paulatto, S. Poncé, D. Rocca, R. Sabatini, B. Santra, M. Schlipf, A. P. Seitsonen, A. Smogunov, I. Timrov, T. Thonhauser, P. Umari, N. Vast, X. Wu, S. Baroni, Advanced capabilities for materials modelling with QUANTUM ESPRESSO. *J. Phys. Condens. Matter* **29**, 465901 (2017).

64. J. P. Perdew, K. Burke, M. Ernzerhof, Generalized gradient approximation made simple. *Phys. Rev. Lett.* **77**, 3865–3868 (1996).

65. T. Tanaka, K. Matsunaga, Y. Ikuhara, T. Yamamoto, First-principles study on structures and energetics of intrinsic vacancies in $SrTiO_3$. *Phys. Rev. B* **68**, 205213 (2003).

66. S. Zhang, J. E. Northrup, Chemical potential dependence of defect formation energies in GaAs: Application to Ga self-diffusion. *Phys. Rev. Lett.* **67**, 2339–2342 (1991).

67. H. Lee, T. Mizoguchi, T. Yamamoto, S. Kang, Y. Ikuhara, First-principles calculation of defect energetics in cubic-$BaTiO_3$ and a comparison with $SrTiO_3$. *Act. Mater.* **55**, 6535–6540 (2007).